

RESEARCH ARTICLE SUMMARY

STRUCTURAL BIOLOGY

Structural basis for inositol pyrophosphate gating of the phosphate channel XPR1

Yi Lu[†], Chen-Xi Yue[†], Li Zhang[†], Deqiang Yao[†], Ying Xia, Qing Zhang, Xinchen Zhang, Shaobai Li, Yafeng Shen, Mi Cao, Chang-Run Guo, An Qin, Jie Zhao, Lu Zhou, Ye Yu*, Yu Cao*

INTRODUCTION: Inorganic phosphate (Pi) is essential for many biological processes, including energy production, signal transduction, and the formation of macromolecules such as DNA and phospholipids. Maintaining appropriate phosphate levels within cells is crucial, as excessive Pi accumulation can lead to harmful effects, such as calcification in vascular and neural systems. In humans, xenotropic and polytropic retrovirus receptor 1 (XPR1) is the only known protein responsible for exporting excess phosphate out of cells. This protein plays a key role in preserving cellular phosphate balance, yet the molecular mechanism behind its function and activation by signaling molecules, such as inositol phosphates (IPs) and inositol pyrophosphates (PP-IPs), remains unclear. Mutations in XPR1 that disrupt phosphate efflux are linked to primary familial brain calcification, a rare neurological disease characterized by the deposition of hydroxyapatite in

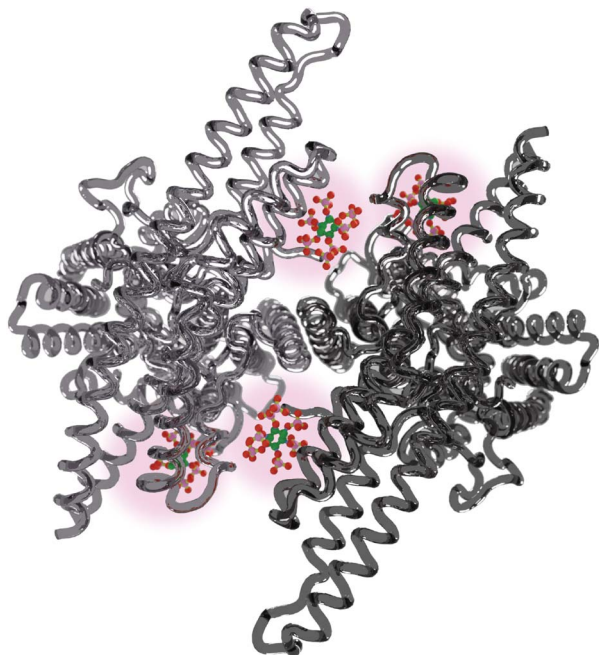
the brain. XPR1 is thus crucial for maintaining phosphate homeostasis, and understanding how it exports phosphate and how cellular signals regulate it is critical for addressing diseases related to phosphate imbalance.

RATIONALE: To investigate the structural and functional properties of XPR1, focusing on how it interacts with PP and IP regulatory molecules, and to reveal the processes that control phosphate efflux, we used cryo-electron microscopy (cryo-EM) and electrophysiological techniques to capture the conformations of XPR1 and monitor its interactions with IPs and PP-IPs.

RESULTS: The present study revealed cryo-EM structures of XPR1 in various conformational states, including its inactive (closed), active (open), and intermediate forms. We demonstrated that XPR1 stays in its closed conformation in the absence of an activator and adapts to its open

conformation upon adding IPs/PP-IPs, with an “all-cross” permeation pathway appearing in its transmembrane domain (TMD) allowing phosphate to flow out of the cell. Two key amino acid residues, W573 and E600 (W, tryptophan; E, glutamic acid), regulate the anion flux, with W573’s bulky side chain influencing channel conformation and E600 providing a negatively charged barrier. Using the competitive Pi-transport inhibitor phosphonoformate, we identified a substrate binding site within the permeation pathway. Additionally, single-channel recordings captured rapid gating events, typified by brief openings and closures, further aligning with channel-like behavior. The study identified two binding sites for IPs and PP-IPs on XPR1—one located between the two SPX (Sgyl/Pho81/XPR1) domains (interSPX site) and another found between the TMD and the SPX domain (TMD-SPX site). Both sites have positively charged surfaces; however, the TMD-SPX site forms a binding pocket much bigger than the interSPX site does, resulting in a preference for polyphosphate inositol with a larger negative surface. Consequently, PP-IPs, particularly IP₇, are more effective than IP₆ at activating XPR1 by binding at both sites, stabilizing the protein in its active form. Electrophysiological experiments showed that XPR1 facilitates phosphate export in a controlled manner, with the binding of IP₇ enhancing this activity notably more than IP₆. Additionally, two intermediate conformations of XPR1 were observed, highlighting the protein’s structural transitions during phosphate transport.

CONCLUSION: This study provides new insights into the mechanism by which XPR1 exports phosphate and how PP-IPs regulate it. The discovery of a second binding site for PP-IPs, along with our structural and functional analysis, explains why PP-IPs are more potent activators of XPR1 than are IPs, offering a clearer understanding of how phosphate homeostasis is maintained in human cells. Additionally, our work characterizes XPR1 as a channel-like protein, enriching the broader understanding of phosphate transport within cells and laying the groundwork for future research into its physiological roles and regulatory mechanisms. These findings provide a molecular and structural basis for understanding disorders related to phosphate metabolism and may inform the development of therapeutic strategies targeting XPR1 to treat such diseases. ■



The human XPR1 structure as viewed from its cytoplasmic side. In this dimeric channel, four highlighted IP₇ molecules are observed, occupying two pairs of activator binding sites: two interSPX sites between the XPR1 subunits and two TMD-SPX sites located laterally.

The list of author affiliations is available in the full article online.

*Corresponding author. Email: yu.cao@shsmu.edu.cn (Y.C.); yuye@cput.edu.cn (Y.Y.)

†These authors contributed equally to this work.

Cite this article as Y. Lu et al., *Science* **386**, eadp3252 (2024). DOI: [10.1126/science.adp3252](https://doi.org/10.1126/science.adp3252)

S READ THE FULL ARTICLE AT
<https://doi.org/10.1126/science.adp3252>

RESEARCH ARTICLE

STRUCTURAL BIOLOGY

Structural basis for inositol pyrophosphate gating of the phosphate channel XPR1

Yi Lu^{1,2†}, Chen-Xi Yue^{3†}, Li Zhang^{1,4†}, Deqiang Yao^{5†}, Ying Xia¹, Qing Zhang^{1,2}, Xinchen Zhang⁶, Shaobai Li¹, Yafeng Shen¹, Mi Cao¹, Chang-Run Guo³, An Qin^{2,7}, Jie Zhao^{2,7}, Lu Zhou⁶, Ye Yu^{3*}, Yu Cao^{1,2*}

Precise regulation of intracellular phosphate (Pi) is critical for cellular function, with xenotropic and polytropic retrovirus receptor 1 (XPR1) serving as the sole Pi exporter in humans. The mechanism of Pi efflux, activated by inositol pyrophosphates (PP-IPs), has remained unclear. This study presents cryo-electron microscopy structures of XPR1 in multiple conformations, revealing a transmembrane pathway for Pi export and a dual-binding activation pattern for PP-IPs. A canonical binding site is located at the dimeric interface of Syg1/Pho81/XPR1 (SPX) domains, and a second site, biased toward PP-IPs, is found between the transmembrane and SPX domains. By integrating structural studies with electrophysiological analyses, we characterized XPR1 as an inositol phosphates (IPs)/PP-IPs-activated phosphate channel. The interplay among its transmembrane domains, SPX domains, and IPs/PP-IPs orchestrates the conformational transition between its closed and open states.

Inorganic phosphate (PO_4^{3-} , Pi) is an essential component of metabolism (1), signal transduction, cellular structures, and genetic material (2–4). However, excessive intracellular Pi can stimulate cell proliferation and mineralization (5), leading to undesirable vascular calcifications in the brain and kidney (6, 7). Therefore, phosphate homeostasis must be strictly regulated. Pi transporters are considered housekeeping genes in cellular phosphate homeostasis (8), and Pi-influx in humans is conducted by members from the sodium-dependent phosphate transporter SLC20 (PiT) and SLC34 (NaPi-II) families (9, 10). Only one phosphate transporter, xenotropic and polytropic retrovirus receptor 1 (XPR1), has been found to be responsible for phosphate efflux in humans. XPR1 (also known as SLC53A1) was named after being identified as the receptor of xenotropic and polytropic mouse leukemia retroviruses (11, 12), and subsequent studies established its exclusive role in orchestrating

Pi efflux (13, 14). In humans, impaired Pi efflux caused by XPR1 mutations leads to PFBC (primary familial brain calcifications), a rare neurological condition characterized by a bilateral pattern of hydroxyapatite deposits in the basal ganglia, dentate nuclei, and thalamus (6, 15).

XPR1 comprises a soluble inositol pyrophosphate-sensor domain at the N-terminal domain, named SPX (Syg1/Pho81/XPR1) (16, 17), and a C-terminal transmembrane helical bundle, postulated to compose the Pi-transporting module. The SPX domain can be found in various Pi-transporters, signaling proteins, and polyphosphate polymerases in eukaryotes (2, 16, 17), but XPR1 is the sole SPX-containing protein in humans. SPX domains can change their conformation upon binding to inositol phosphates (IPs) and inositol pyrophosphates (PP-IPs), a class of signaling molecules whose level indicates the cellular Pi abundance (2, 17–19). Some studies show strong evidence that IPs and PP-IPs, such as IP₆, IP₇, and IP₈, can bind to SPX of XPR1 (14, 20), and inhibition of IP₇ and IP₈ synthesis by IP₆ kinases *IP6K1* and *IP6K2* inhibitors leads to lower 5-IP₇ levels and reduced XPR1-mediated phosphate efflux (21). Therefore, XPR1 could catalyze a pyrophosphates-gated phosphate efflux to mediate cellular phosphate homeostasis (2, 14, 15).

This study presents cryo-electron microscopic (cryo-EM) structures of human XPR1 in varying operational states, encompassing inward-facing, channel-open, and intermediate conformations. Our electrophysiological studies show that XPR1 functions as an IPs/PP-IPs-activated phosphate channel or channel-like transporter. We observed conformational changes within the SPX domain upon its engagement with IPs/PP-IPs and propose a gating mechanism for PP-IPs-activated Pi-efflux.

XPR1 functions as an IPs/PP-IPs-activated phosphate channel

To assess the permeation of inorganic phosphate through XPR1, we used a controlled experimental setup, ensuring that both the bath solution and the recording pipette were saturated with 100 mM Pi. To activate XPR1, 1 mM inositol hexakisphosphate (IP₆) was introduced into the pipette. Subsequently, a voltage step protocol was applied, ranging from -180 mV to +100 mV in 20-mV increments every 100 ms (Fig. 1A). This protocol was designed to maximize the driving force for Pi flux, thereby providing a comprehensive evaluation of Pi permeation.

Including 1 mM IP₆ within the intracellular milieu augmented the permeation of Pi facilitated by XPR1, with the maximal current densities observed at -180 mV ($I_{\max}^{-180 \text{ mV}}$) reaching -47.7 ± 19.3 and -96.2 ± 28.4 pA/pF, in the absence and presence of 1 mM IP₆, respectively. Adding 50 mM of phosphonoformate (PPF)—a competitive Pi-transport inhibitor (22, 23)—alongside 1 mM IP₆ intracellularly resulted in an attenuation of XPR1-mediated Pi transport across the cellular membrane, as evidenced by the recorded $I_{\max}^{-180 \text{ mV}}$ of -57.5 ± 32.8 pA/pF (Fig. 1B). By contrast, control experiments conducted on human embryonic kidney 293T (HEK293T) cells transfected with a plasmid devoid of the XPR1 gene and subjected to identical experimental conditions exhibited negligible Pi permeation in response to intracellular 1 mM IP₆ ($I_{\max}^{-180 \text{ mV}} = -23.2 \pm 8.4$ and pA/pF, -25.2 ± 4.5 with and without 1 mM IP₆, respectively). These findings indicated the pivotal role of XPR1 in mediating phosphate efflux across the cell membrane, thereby suggesting its functionality as a phosphate channel or a channel-like transporter.

Cryo-EM analysis of human XPR1 proteins

XPR1 consists of an N-terminal soluble SPX domain (fig. S1), followed by a transmembrane helical bundle and a short, disordered C-terminal domain (2, 17). Human XPR1 (hXPR1) proteins were successfully produced with a HEK293-based system. In brief, Expi293F cells were transiently transfected with expression vectors derived from pcDNA3.4 carrying the cDNA of hXPR1, tagged with a C-terminal Flag affinity tag. Initial attempts at purification using *n*-dodecyl-β-D-maltoside (DDM) as detergent in solubilization failed to yield proteins with sufficient stability and homogeneity as evaluated by size-exclusion chromatography (SEC) (fig. S2). Subsequent optimization efforts demonstrated that the use of lauryl maltose neopentyl glycol (LMNG) in solubilization, coupled with SEC performed using glyco-diosgenin (GDN) as the detergent in the mobile phase, improved stability and homogeneity. During purification, human XPR1 formed stable homodimers, as confirmed by SEC profiles and 200-kV cryo-EM analysis (FEI, Talos Arctica). Cryo-EM images

¹Institute of Precision Medicine, the Ninth People's Hospital, Shanghai Jiao Tong University School of Medicine, Shanghai 200125, China. ²Department of Orthopaedics, Shanghai Key Laboratory of Orthopaedic Implant, Shanghai Ninth People's Hospital, Shanghai Jiao Tong University School of Medicine, Shanghai 200011, China. ³School of Basic Medicine and Clinical Pharmacy and State Key Laboratory of Natural Medicines, China Pharmaceutical University, Nanjing 211198, China. ⁴Department of Physiology, The University of Texas Southwestern Medical Center, Dallas, TX 75390, USA. ⁵Institute of Aging & Tissue Regeneration, Renji Hospital, School of Medicine, Shanghai Jiao Tong University, Shanghai 200127, China. ⁶Department of Medicinal Chemistry, School of Pharmacy, Fudan University, Shanghai 201203, China. ⁷Shanghai Frontiers Science Center of Degeneration and Regeneration in Skeletal System, Shanghai Ninth People's Hospital, Shanghai Jiao Tong University School of Medicine, Shanghai 200011, China.

*Corresponding author. Email: yu.cao@shsmu.edu.cn (Y.C.); yuye@cpu.edu.cn (Y.Y.)

†These authors contributed equally to this work.

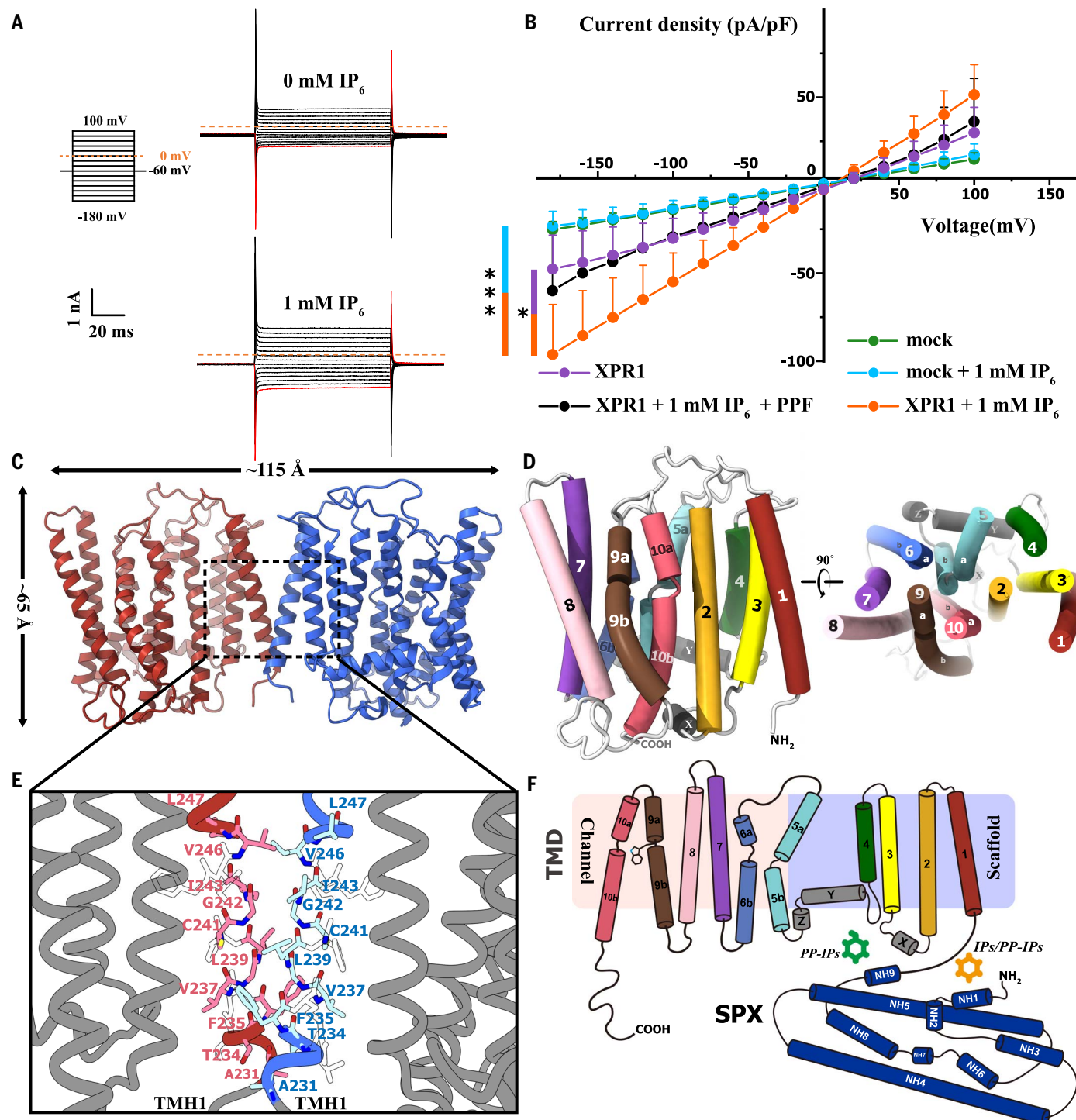


Fig. 1. The anion currents by human XPR1 and the cryo-EM structure of hXPR1 apo. (A and B) The protocol [(A), left], typical traces [(A), right], and pooled data (B) corresponding to the step-voltage protocol, ranging from -180 mV to +100 mV with a 20-mV increase every 100 ms interval to characterize the current-voltage (*I*-*V*) relationship of Pi permeation (mean \pm SE, $n = 5$ independent experiments). * $P < 0.05$, ** $P < 0.01$, *** $P < 0.001$, two-way analysis of variance (ANOVA) followed by Tukey's multiple comparison test, $F(56, 300) = 1.4$; $P = 1.00$ for mock versus mock-IP₆, $P = 0.0001$ for XPR1-IP₆ versus mock-IP₆, $P = 0.08$ for XPR1 versus XPR1-IP₆, and $P = 0.01$ for XPR1-IP₆ versus XPR1-IP₆/PPF; $P = 0.0001$ for mock-IP₆^{-180 mV} versus XPR1-IP₆^{-180 mV},

and $P = 0.03$ for XPR1^{-180 mV} versus XPR1-IP₆^{-180 mV}. (C) The dimeric hXPR1 apo structure is depicted as a cartoon model and colored in red and blue for the two protomers. (D) The arrangement of the transmembrane and intracellular helices in the hXPR1 TMD. (E) The dimeric interface at the TMDs of hXPR1. The enlarged view shows the contacting residues from the TMH1 helices of two protomers of hXPR1. Single-letter abbreviations for the amino acid residues are as follows: A, Ala; C, Cys; D, Asp; E, Glu; F, Phe; G, Gly; H, His; I, Ile; K, Lys; L, Leu; Q, Gln; R, Arg; T, Thr; V, Val; W, Trp; and Y, Tyr. (F) The cartoon representation of the TMD topology of the hXPR1 monomer. The transmembrane helices have the same color scheme as shown in (D).

were collected using a Titan Krios transmission electron microscope (FEI) operating at 300 kV, with data processing conducted using RELION-4 and cryoSPARC (24, 25). Both two-dimensional (2D) and 3D classification on hXPR1 particles purified without additives [hXPR1 apolipoprotein (apo)] revealed strong signals for transmembrane domains (TMDs), whereas the electron density for the soluble SPX domain remained weak and discontinuous (fig. S3). Addition of substrate Pi showed no improvement in the SPX domain map quality, and the introduction of the potentiator hexaphosphate (IP₆) slightly enhanced the signal (fig. S4), indicating a potential IP₆-induced conformational change. Nevertheless, the local map quality of SPX was not sufficient to solve the structure of full-length hXPR1. To enhance conformational stability, we replaced Pi with PPF and added it with IP₆ into hXPR1 protein samples (hXPR1-PPF/IP₆). Cryo-EM analysis revealed a complete electron map with improved signals for the SPX domain (fig. S5). Further refinement and polishing generated final EM maps with an overall resolution of 4.16 Å for full-length hXPR1-IP₆/PPF, 3.68 Å for hXPR1 apo, and 3.41 to 3.57 Å for hXPR1-IP₆ as a TMD only (figs. S3 to S5). Molecular models were built in the corresponding EM maps, using the hXPR1 structural model predicted by AlphaFold as the starting model (<https://alphafold.ebi.ac.uk/entry/Q9UBH6>). To address the different effects between IP₆ and PP-IPs, chemoenzymatically synthesized IP₇ was added to XPR1, resulting in an EM map of 2.84-Å resolution with improved signals for both TMD and SPX domain (fig. S6). Tetrahedral anions sulfate, vanadate, and tungstate were tested to explore stabilizing effects. The supplementation of tungstate (hXPR1-WO₄/IP₆) resulted in high-resolution cryo-EM maps with a determined structure at 3.65 Å (fig. S7). Unless otherwise specified, the hXPR1-IP₇ structure was primarily used in the structural analysis.

Overall architecture of XPR1 transmembrane domain

The hXPR1 apo structure revealed a homodimeric arrangement of TMDs (Fig. 1, C and E, and fig. S8A). Because of poor electron density quality, the N-terminal residues 1 to 227 and the disordered C-terminal region (620 to 696) were left unmodeled. The monomeric XPR1 TMD is characterized by 10 transmembrane helices (TMH1 to 10) and three intracellular helices (inH_X to z), connected by various loops. Notably, TMH5, 6, 9, and 10 show tilting and distortion, featuring a break in the middle of the membrane region (Fig. 1, D and F). The three nontransmembrane helices, inH_X to z, were all located at the cytoplasmic side of the TMD, with the lengthy inH_Y positioned near the lipidic layer and cytosol border, parallel to the membrane plane. The dimeric interface involves TMH1 from both protomers, primarily mediated

by hydrophobic interactions (Fig. 1E). The limited dimeric contacts within the TMDs suggest that the stability of XPR1 dimerization may also involve contributions from the SPX domains.

Conformational changes induced by IPs binding

Upon supplementation with IP₆, hXPR1 maintains its dimeric overall architecture (Fig. 2A and fig. S8B), including dimeric TMDs and some discontinuous electron density corresponding to the unsolved SPX domains. A contiguous and flat region of electron density lacking proteinaceous features was observed on each protomer near the dimeric interface (fig. S8B), potentially representing a cholesterol hemisuccinate (CHS) molecule, which was introduced during the purification process.

Structural superposition between the protomers A and B in hXPR1-IP₆ dimer unveils differing conformations (Fig. 2B). Protomer B (hXPR1-IP₆^B) adopts the same conformation as in hXPR1 apo, but protomer A (hXPR1-IP₆^A) displays a break between TMH9a and 9b at residue W573, resulting in a pronounced outward displacement of TMH9a while TMH9b remains largely unchanged (Fig. 2, C and D). Comparison of hXPR1 apo and hXPR1-IP₆^B identified an inward-facing chamber formed by TMH5b, 6b, 7, 8, and 9, extending deeply into hXPR1 TMD and domed by tilting TMH9a and residue W573 (Fig. 2C). By contrast, hXPR1-IP₆^A structure shows the removal of TMH9a and residue W573 from its original location, resulting in the absence of the inward-facing chamber (Fig. 2D). Consequently, a transmembrane channel appears, replacing the inward-facing chamber. These distinct conformations are designated as hXPR1^{TF}—characterized by the presence of an inward-facing chamber (hXPR1 apo and hXPR1-IP₆^B)—and hXPR1^{open}, characterized by the formation of a transmembrane channel (hXPR1-IP₆^A).

Subsequent 2D and 3D classifications of cryo-EM particles reveal a complex landscape of multiple conformations within the hXPR1-IP₆ complex, including homodimeric hXPR1^{open}, homodimeric hXPR1^{TF}, and an asymmetric dimer with both hXPR1^{TF} and hXPR1^{open} states (fig. S4 and table S1). These states were resolved at resolutions ranging from 3.41 to 3.57 Å, and this conformational heterogeneity hints at an interplay between hXPR1 and IP₆, suggesting an IPs/PP-IPs-induced channel-open mechanism for phosphate conductance.

Substrate binding site and IPs binding interface (interSPX site)

The hXPR1 apo and hXPR1-IP₆ structures provide insights into the conformational changes induced by IP₆. However, the mechanism of gating by ligands remains elusive in the absence of the SPX domain in these structures. Although there is a prior crystal structure of

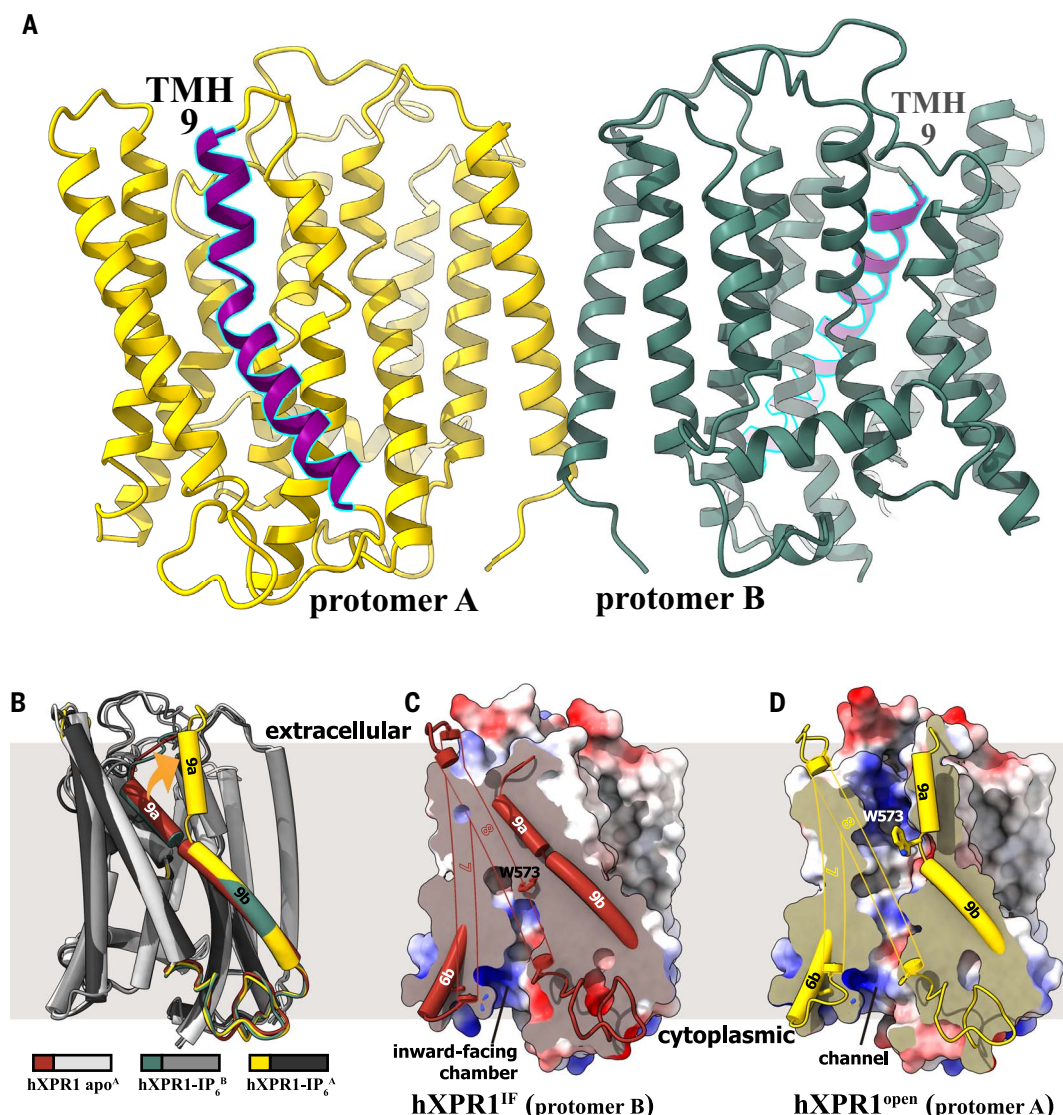
the hXPR1 SPX domain, it does not include PP-IPs (17). We speculated that the binding of IP₆ could initiate the conformational shift between hXPR1^{TF} and hXPR1^{open} states, thus preventing structure determination of the SPX domain in a stable conformation. To minimize conformational changes upon IP₆ addition, we supplemented inhibitor PPF in the hXPR1-IP₆ sample. The resulting 2D classification revealed complete EM signals including both SPX regions and TMDs of hXPR1 (fig. S5A), enabling the determination of full-length hXPR1 (hXPR1-IP₆/PPF), except for the disordered C-terminal region (residues 621 to 696), which remained unmodeled.

The cryo-EM map for hXPR1-IP₆/PPF exhibited C2 symmetry, with the twofold axis at the center of the dimeric interface perpendicular to the membrane plane (Fig. 3A and fig. S8C). The two SPXs are located at the cytoplasmic side of TMDs, forming a bundle of helices (NH1–9) in a fold similar to the SPX structures reported previously (Fig. 1F and fig. S9). The TMDs of hXPR1-IP₆/PPF were in the hXPR1^{TF} state, and further analysis identified a blob of nonproteinous electron density deep in the inward-facing chamber (Fig. 3C). Although the noise level in the EM map of XPR1-PPF/IP₆ is relatively high, a comparison between local EM maps of XPR1 apo and XPR1-PPF/IP₆ showed that no density is observed at the corresponding position in the XPR1 apo map (fig. S10), suggesting a potential site for PPF binding. Residue W573, crucial for the conformation transition of TMH9, was situated next to the density in the cavity. Functional assays involving point mutations at these coordinating residues [K482A (K482→A), R570A, R603A, and R604A] within the substrate binding site demonstrated a pronounced reduction in IP₆-stimulated Pi efflux through XPR1 (Fig. 3E and fig. S10D), with significant changes in their $I_{max}^{-180 \text{ mV}}$ in response to intracellular 1 mM IP₆ (35.82 ± 8.54 , -21.26 ± 5.76 , -40.46 ± 20.08 , and $-50.24 \pm 19.06 \text{ pA/pF}$, for K482A, R570A, R603A, and R604A, respectively), underscoring the role of this putative substrate binding site in mediating efficient Pi efflux through XPR1.

In the crystal structure of the SPX domain of hXPR1 (17), two copies of SPX formed a dimer with an interface comprising helices NH4 and NH6 from both protomers (fig. S9A). However, in the hXPR1-IP₆/PPF structure, NH4 and NH6 are positioned away from the C2-symmetric center, excluding them from dimerization. Instead, a “noncontacting” dimeric interface is formed, including two identical subregions. Each subregion consists of NH1 and NH5 from one SPX domain and NH9 from the adjacent SPX domain (Fig. 3A). The SPX interface is rich in positively charged residues, such as K2 in NH1, K158/161/162/165 in NH5, and R211 and K213/216 in NH9 (Fig. 3B and fig. S9C). The shortest distance between two SPX domains is about 6.9 Å (K165 to R211), precluding the possibility of direct interactions. Instead, the dimerization is bridged

Fig. 2. hXPR1 in closed (inward-facing) and channel-open conformations.

(A) The hXPR1 structure is depicted as a cartoon model with molecular models for protomers A and B colored in yellow and green, respectively, except for the helix TMH9, which is highlighted in purple. **(B)** A superposition of the structures of hXPR1 apo^A (light gray), hXPR1-IP₆^A (gray), and hXPR1-IP₆^B (black). The structures are depicted as cylindrical cartoon models, and the TMH9 helices in superposition are colored in red, yellow, and green for hXPR1 apo^A, hXPR1-IP₆^A, and hXPR1-IP₆^B, respectively. **(C)** The inward-facing chamber in the hXPR1^{IF} state. The hXPR1 apo^A structure is shown as a cylindrical cartoon model with solvent-accessible electrostatic surface-potential maps sliced to show the inward-facing chamber. Part of the cartoon model for TMH7 and 8 is transparent for clear observation. **(D)** The channel in the hXPR1^{open} state. hXPR1-IP₆^A is viewed at the same angle as in (C) and shown as a cylindrical cartoon model with solvent-accessible electrostatic surface-potential maps sliced to show the transmembrane channel. Part of the cartoon model for TMH7 and 8 is transparent for clear observation.



Downloaded from https://www.science.org at University Van Amsterdam on April 13, 2025

by the IP₆ molecules identified within the subregions of the SPX interface. The EM analysis revealed two lumps of nonproteinous electron density in both subregions (hereafter “interSPX site”), and the IP₆ molecules were modeled in the electron density (Fig. 3B). The negatively charged phosphate groups of the ligand are surrounded by and make electrostatic interactions with positively charged residues (K2, K158, K161, K162, K165, and R211) (Fig. 3B), highlighting the crucial role of IP₆ in stabilizing SPX dimerization in hXPR1. Mutation analysis further elucidated the importance of these interactions. The double mutant XPR1^{R211A/R219A} resulted in the abolition of the enhanced Pi efflux mediated by XPR1 in the presence of IP₆ (Fig. 3D), with $I_{max}^{-180\text{ mV}}$ showing no significant difference between conditions with and without 1 mM IP₆ (-49.4 ± 13.1 and -35.6 ± 10.7 pA/pF, respectively, $P > 0.05$).

In light of the observed IP₆ bridge between the positively charged residues at the interface,

the double mutation R211E/R219E was engineered to reduce the repulsive forces exerted by R211/R219 against the opposing residues K161/K152/K165. The XPR1^{R211E/R219E} mutant exhibited Pi efflux currents in the absence of 1 mM IP₆ that were comparable to those of wild-type (WT) XPR1 upon IP₆ treatment ($I_{max}^{-180\text{ mV}} = -118.5 \pm 25.3$ pA/pF), and the addition of 1 mM IP₆ further amplified the Pi efflux ($I_{max}^{-180\text{ mV}} = -168.4 \pm 76.2$ pA/pF) (Fig. 3D). Substitution of these negatively charged acidic residues at positions 211 and 219 may facilitate the formation of interSPX contacts, effectively mimicking the binding and activation effect of IP₆ on XPR1, thereby promoting Pi efflux even in the absence of IP₆.

The PP-IPs binding interface (TMD-SPX site)

PP-IPs, such as IP₇ or IP₈, are reported to be more potent activators for SPX-containing proteins than IP₆ (17, 26). To understand PP-IPs’ enhanced activating effects, we chemoenzymatically synthesized PP-IP (27), majorly IP₇ (fig.

S2B), and solved the structure of XPR1 bound with IP₇ (fig. S6). Whereas the SPX domain was unresolved in XPR1-IP₆ (fig. S6), cryo-EM analysis of XPR1-IP₇ showed strong signals for both the TMD and SPX domains upon supplementation with IP₇, resulting in a full-length structure of XPR1-IP₇ determined at about 2.84 Å resolution. The overall folding of XPR1-IP₇ closely resembles that of XPR1-PPF/IP₆, with TMDs in both structures adopting the closed (inward-facing) conformation. In addition to the nonproteinous densities in the interSPX sites of XPR1-IP₇, two additional blobs of map densities were identified between the TMD and SPX domains (fig. S8D). This additional density suggests the existence of a PP-IP-specific binding site (TMD-SPX site) comprising NH5, NH9, inHY, and the loop connecting inHY and TMH4 (Fig. 4, A and B). Similar to the interSPX site, the TMD-SPX site is a positive charge-rich subregion. Lysine and histidine residues are located on both the TMD and SPX sides, including

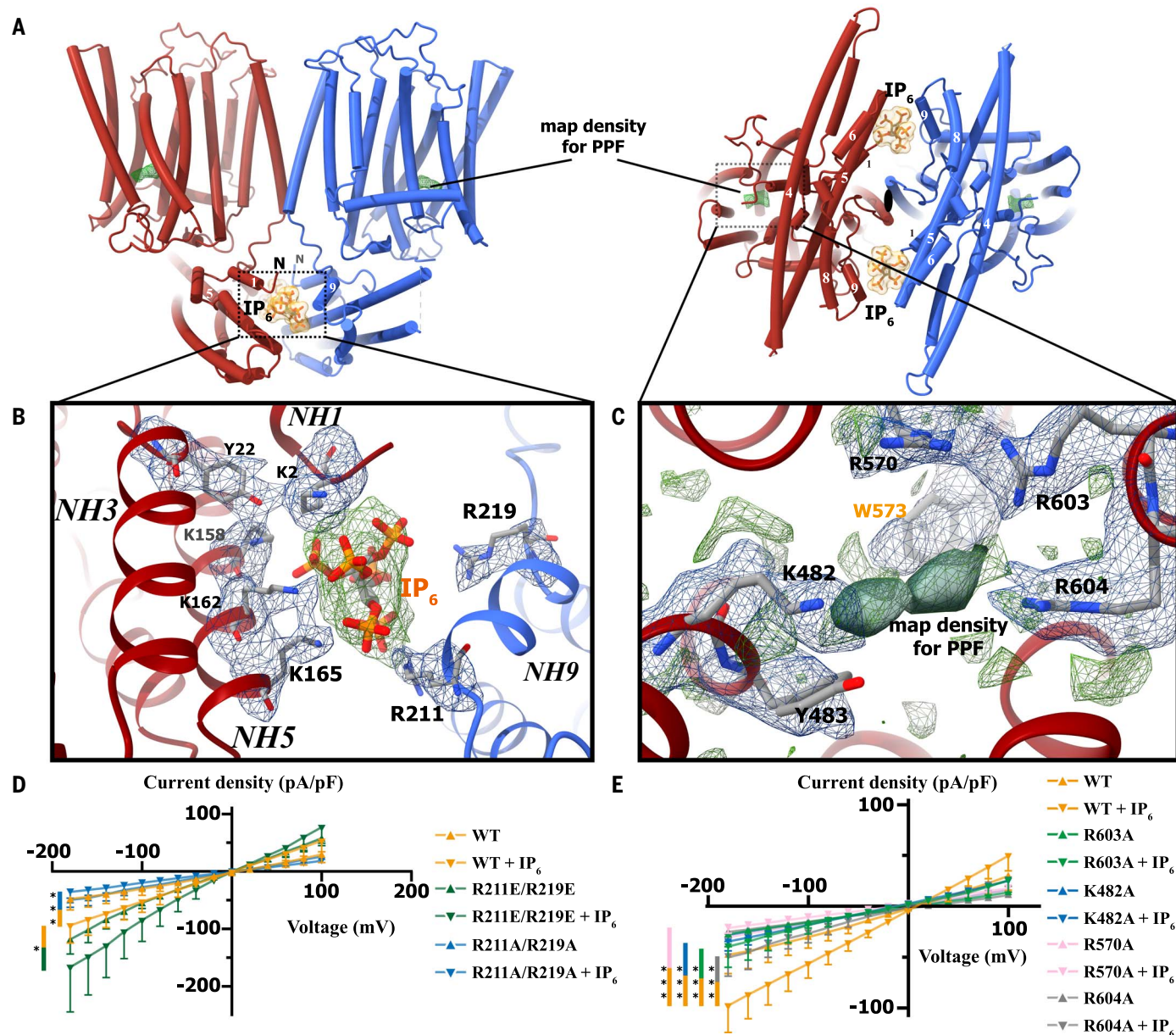


Fig. 3. The full-length structure of hXPR1-IP₆/PPF. (A) The hXPR1 structure is depicted as a cartoon model and viewed at the same angle as shown in Fig. 1C. The IP₆ molecules are shown as stick models colored by elements (carbon, gray; oxygen, red; phosphorus, orange; nitrogen, blue), which are enclosed in transparent surface models. (B) The enlarged view for the IPs/PP-IPs binding pocket. IP₆ is shown as a ball-and-stick model colored by elements [as described in (A)], and the contacting residues are shown as stick models. (C) The enlarged view for the putative PPF binding site. Residues adjacent to additional density are shown as stick models. In (B) and (C), the nonproteinous EM map density is shown as green mesh, and the density enclosing the interactive residues is shown as blue mesh. The density enclosing the putative PPF binding site is highlighted as a green surface. (D) The I-V relationship of Pi permeation in cells expressing XPR1 WT, XPR1^{R211A/R219A}, and

XPR1^{R211E/R219E} (mean \pm SE, $n = 5$ independent experiments). * $P < 0.05$, ** $P < 0.01$, *** $P < 0.001$, two-way ANOVA with Tukey's multiple comparison test, $F(70, 360) = 1.7$; $P = 0.2$ for XPR1 WT versus XPR1^{R211E/R219E}, $P > 1.0$ for XPR1 WT versus XPR1^{R211A/R219A}, $P < 0.0001$ for XPR1 WT-IP₆ versus XPR1^{R211A/R219A}-IP₆, $P = 0.03$ for XPR1 WT-IP₆ versus XPR1^{R211E/R219E}-IP₆, $P = 1.0$ for XPR1^{R211A/R219A} versus XPR1^{R211A/R219A}-IP₆, and $P = 0.1$ for XPR1^{R211E/R219E} versus XPR1^{R211E/R219E}-IP₆; $P < 0.0001$ for XPR1-IP₆^{-180 mV} versus XPR1^{R211A/R219A}-IP₆^{-180 mV}, and $P = 0.04$ for XPR1-IP₆^{-180 mV} versus XPR1^{R211E/R219E}-IP₆^{-180 mV}. (E) The I-V relationship of Pi permeation in cells expressing XPR1 WT and XPR1^{R603A}, XPR1^{K482A}, XPR1^{R570A}, and XPR1^{R604A}. *** $P < 0.001$, two-way ANOVA with Tukey's multiple comparison test, $F(126, 600) = 1.7$. The XPR1 WT curves, depicted in Fig. 1B with or without 1 mM IP₆, are refigured in Fig. 3, D and E for comparative analysis.

H125, K129, and K132 from the SPX domain and K364, K368, K369, and K376 from the TMD (Fig. 4C and fig. S11B). Structural analysis of the TMD-SPX site provides insight into its binding preference for inositol pyrophosphate over inositol phosphate. The distance between the sur-

faces in the TMD-SPX site ranges from 10 to 12 Å, much longer than the 6- to 8-Å distance in the interSPX site (fig. S11, C and D). This spatial configuration suggests that the TMD-SPX site is more suitable for accommodating the larger pyrophosphate groups of IP₇ and IP₈. Support-

ing this conclusion, the apparent affinity of IP₇ was more than 20-fold higher than that of IP₆, with half-maximal response concentrations (EC₅₀) measured at 0.372 ± 0.06 mM for IP₇ and 7.72 ± 8.16 mM for IP₆ (free acid) in inside-out macropatch recordings (Fig. 4E).

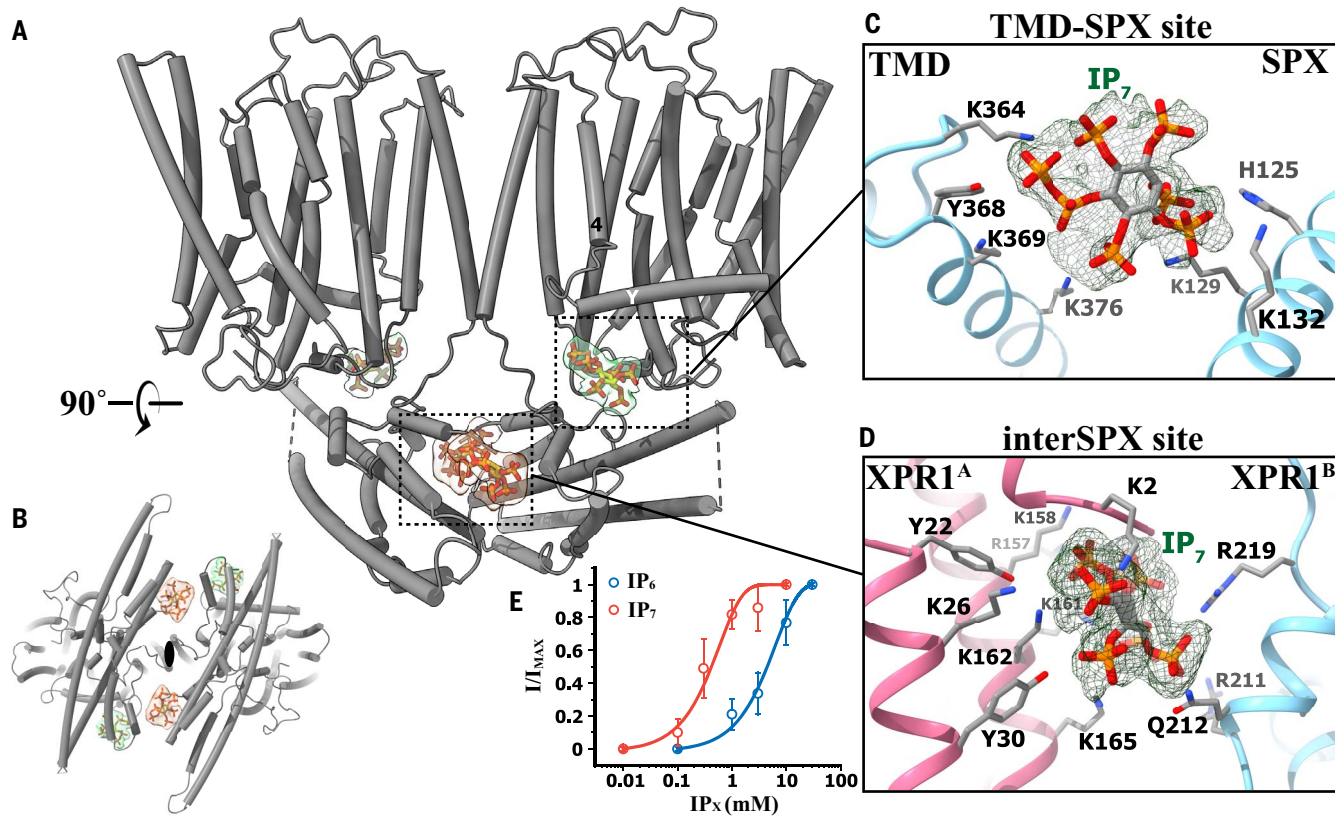


Fig. 4. The dual-binding pattern for IP₇ in hXPR1. (A) Cryo-EM structure of XPR1-IP₇. The IP₇ molecules bound at the dimeric interface of SPX domains (interSPX site) are shown as stick models enclosed by the EM map density in orange, and the IP₇ molecules bound between the TMD and SPX domain (TMD-SPX site) are shown as stick models enclosed by the EM map density in green. (B) The cryo-EM structure of XPR1-IP₇ viewed from the intracellular side of the cell membrane. (C) An enlarged view of the TMD-SPX site. (D) An enlarged view of the interSPX site. (E) Concentration-response curves for IP₆- and IP₇-induced currents were obtained from inside-out macropatch recordings in HEK293T cells expressing XPR1. The data were fitted to the Hill equation and are presented as mean \pm SEM, with $n = 3$ to 4 independent experiments.

The phosphate permeation pathway in hXPR1

The structural analysis of hXPR1 in its open and closed conformations revealed a potential permeation pathway across the membrane. In the hXPR1^{open} conformation, the pathway is characterized by hydrophilic residues arranged in a positive-negative-positive-negative-positive charge pattern, with the positively charged zones potentially serving as phosphate binding sites (Fig. 5A and fig. S12A). The central positively charged zone, comprising residues K482, R570, R603, and R604, is also the site highlighted previously as putatively involved in PPA binding. The pathway also includes two acidic spacers, one formed by residues D398, D529, and D533 between the inner and central zones and another smaller spacer formed by E600 between the central and outer zones. The pore-radius analysis indicated that the E600 side-chain rotation during the transition to the hXPR1 closed state constricts the pore, emphasizing its role in anion permeation (Fig. 5B). Electrophysiological assays of the hXPR1^{E600A} mutant revealed that Pi efflux occurred even without IP₆ ($I_{max}^{-180} mV$ of -93.6 ± 22.9 pA/pF for hXPR1^{E600A} without IP₆ versus -96.2 ± 28.4 pA/pF for WT hXPR1 with 1 mM IP₆), sug-

gesting that E600 acts as a gate for Pi permeation (Fig. 5C). Single-channel recordings provided additional evidence for the channel-like behavior of XPR1, with rapid gating events indicative of ion channel activity and conductance levels between 10 and 15 pS (Fig. 5D).

The mechanistic implication for IPs/PP-IPs-activated phosphate efflux

The crucial role of the inhibitor PPF in solving the full-length structure of hXPR1 suggested the potential to capture intermediate conformations of hXPR1 with suboptimal substrates. hXPR1 EM samples were thus supplemented with anions with a tetrahedral arrangement. Neither SO₄²⁻ nor VO₄³⁻ additions produced cryo-EM data of sufficient quality to determine a structure, but hXPR1 supplemented with WO₄²⁻ and IP₆ (hXPR1-IP₆/WO₄) generated particles with full-length structural features in 2D and 3D classification (fig. S7). The hXPR1-IP₆/WO₄ structure was solved at 3.65 Å; however, the local resolution of SPX domain is not ideal (about 3.8 to 4.8 Å), but local refinement generated a 4.59-Å resolution map of this region. Although the overall resolution was impaired compared with the original map, the signals

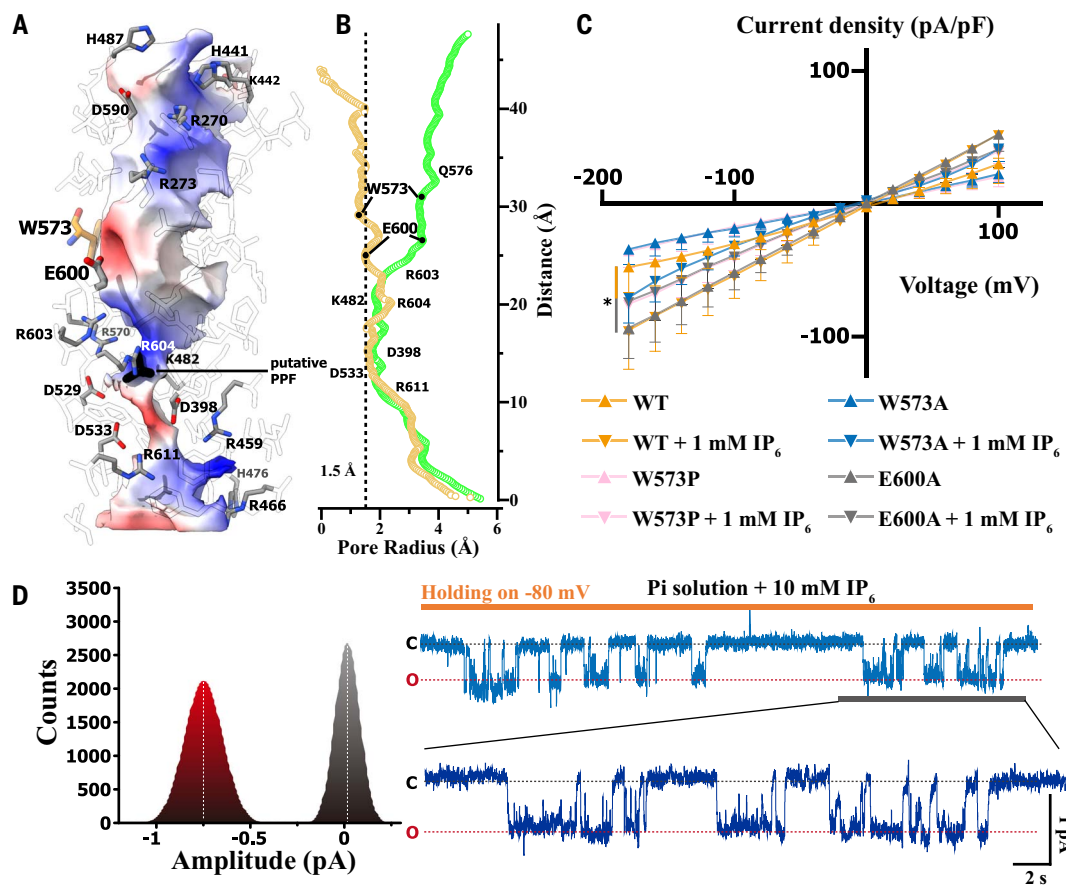
for the SPX domain were greatly improved, allowing for model building (fig. S14).

Unlike hXPR1-IP₆/PPF, hXPR1-IP₆/WO₄ was characterized as TMDs in open conformations similar to hXPR1-IP₆ (Fig. 6A and fig. S8E) and to a SPX dimer in a “twisted” conformation when compared with that in hXPR1-IP₆/PPF (Fig. 6B). Structural superposition of the TMDs from hXPR1 in different states revealed that the two protomers in hXPR1-IP₆/WO₄ are slightly different from each other and that both adapt into intermediate conformations close to the hXPR1^{open} state (Fig. 6C), hereafter designated “hXPR1^{interA}” (protomer A) and “hXPR1^{interB}” (protomer B), respectively. On the basis of its structural similarity to phosphate, tungstate, although not an ideal substrate for hXPR1, might pass through the phosphate channel with relatively lower permeability. This results in TMD conformations characterized by all-pass channels, with the gating residues W573 and E600 “paused” halfway between their respective conformations in the hXPR1^{IF} and hXPR1^{open} states (Fig. 6C).

Maintaining a dimeric conformation, the SPX domains hXPR1-IP₆/WO₄ are pulled away from their original central location in C2-symmetric

Fig. 5. The permeation pathway of hXPR1. (A) Residues outlining the interior surface in hXPR1^{open} are shown as stick models, and the crucial residues are colored by element. The black line represents the position corresponding to additional density interpreted as PPF in the XPR1-PPF/IP₆ structure. The interior spaces in hXPR1^{open} were calculated with HOLLOW (44) and are shown as solvent-accessible electrostatic surface-potential maps. (B) The pore radius for the inner pathways as calculated by HOLE. The green circles show the radius for transmembrane channel in hXPR1^{open}, and the tan circles show the radius for the inward-facing chamber in hXPR1^{IF}.

(C) The I-V relationship of Pi permeation in cells expressing XPR1 WT and XPR1^{W573A}, XPR1^{W573P}, and XPR1^{E600A}. *P < 0.05, two-way ANOVA with Tukey's multiple comparison test, F(98, 480) = 1.2; P = 0.8 for XPR1^{W573A} versus XPR1^{W573A}-IP₆; P = 0.1 for XPR1^{W573P} versus XPR1^{W573P}-IP₆, and P = 0.9 for XPR1^{E600A} versus XPR1^{E600A}-IP₆; P = 1.0 for XPR1^{-180mV}-IP₆ versus XPR1^{-180mV}, and P = 0.05 for XPR1^{-180mV} versus XPR1^{E600A}, -180mV. The WT XPR1 curves, presented in Fig. 1B with or without adding 1 mM IP₆, were refigured in Fig. 5C for comparative analysis. (D) Single-channel recordings of XPR1 were performed in an inside-out configuration at a holding potential of -80 mV (right). Gaussian fitting was applied to all-point histograms, corresponding to open (O, red) and closed (C, black) states (left).



hXPR1-IP₆/PPF (Fig. 6, A and B), “hanging” askew at the cytoplasmic side of the hXPR1 TMDs as the result of a sliding displacement. When superposed with the SPX dimer from the hXPR1-IP₆/PPF structure, the two SPX domains hXPR1-IP₆/WO₄ both move away from the C2 axis, making the overall shape extended by about 30 Å (Fig. 6D). As a result, the two IPs/PP-IPs binding pockets fall apart, and thus no IP₆ density was found in hXPR1-IP₆/WO₄.

Discussion

On the basis of the TMD and SPX conformations revealed by hXPR1 supplemented with various functional molecules, we propose an IPs/PP-IPs-activated phosphate conductance mechanism for XPR1 (fig. S16). When intracellular Pi levels are low, the absence of IPs/PP-IPs binding disrupts SPX dimerization. Consequently, the TMDs of XPR1 stabilize in the hXPR1^{IF} conformation as the resting state, thereby preventing phosphate efflux. Upon elevation of Pi levels, IPs/PP-IPs bind to the SPX domains, triggering a transition to the C2-symmetric configuration with dimerized SPX domains, which is primed to shift into the

hXPR1^{open} state and facilitate rapid phosphate efflux. The occupancy of the TMD-SPX site by PP-IPs further stabilizes the C2-symmetric configuration of XPR1, reinforcing its Pi-conductance state and enhancing Pi efflux. As Pi levels decrease, the dissociation of IPs/PP-IPs causes the disassembly of the SPX domains, returning XPR1 to its resting state.

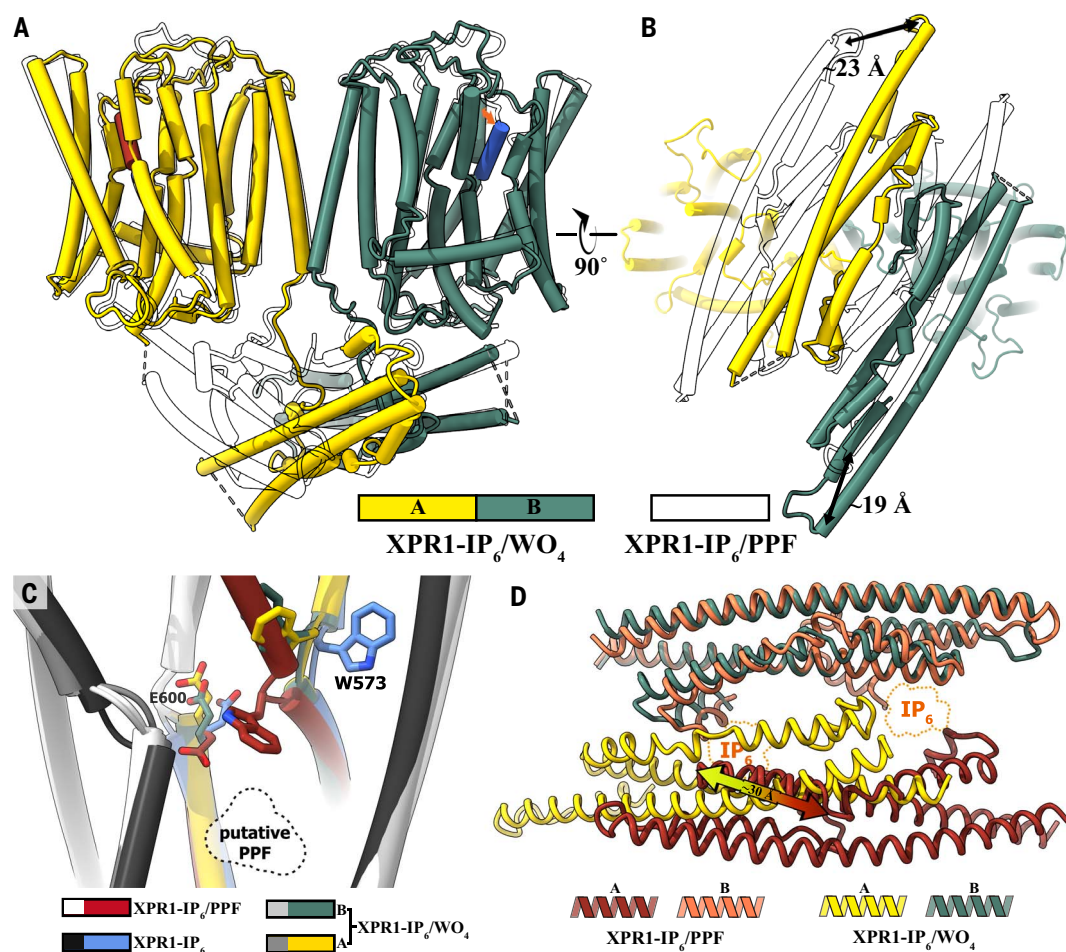
XPR1 functions as the exclusive phosphate exporter in humans and is structurally distinct from previously characterized phosphate transporters (28, 29). Searches for structurally related transporters using the Protein Data Bank (PDB) based on either sequence similarity or structural similarity have yielded no reliable matches. Using the PDBeFold service (<https://www.ebi.ac.uk/msd-srv/ssm/>), we identified that channelrhodopsin, a group of light-gated ion channels, shares some structural similarities with human XPR1. Although the protein sequence alignment showed low identity (about 23.4%), a structural superposition aligns hXPR1 well with ChRmine, a channelrhodopsin from *Rhodomonas lens* (30), using TM5-10 of XPR1 and TM2-7 of ChRmine as references in the structural alignment with a root mean square

deviation of 8.776 Å (fig. S17). Additionally, two pairs of structurally related residues in the superposition, W573^{XPR1}-W223^{ChRmine}, and E600^{XPR1}-K257^{ChRmine}, were all established as crucial residues in their respective structures (30, 31), supporting the idea that XPR1 might conduct the Pi efflux in a channel-like manner.

Inositol polyphosphates regulate XPR1 Pi transport, with PP-IPs serving as a signal indicating high phosphate load within cells. Despite its initial classification as a transporter in the solute carrier family (encoded by gene *SLC53A1*), electrophysiology experiments suggest a channel-like mechanism for XPR1, which is corroborated by cryo-EM structures revealing the presence of a putative phosphate channel in the TMD of XPR1. This channel-like mechanism for SLC family members could also be found in urea transporter (*SLC14A1* and *SLC14A2*) (32, 33), ensuring rapid substrate translocation across cell membranes. In the HEK293T cell overexpression system, distinct from oocyte models (34), Pi efflux currents were measured at approximately 100 pA/pF, indicating a swift transit of Pi across the permeation pathway. Additionally, single-channel recordings captured rapid

Fig. 6. The intermediate conformations in hXPR1-IP₆/WO₄.

(A and B) The structure of hXPR1-IP₆/WO₄ is shown as a cylindrical cartoon model superposed with hXPR1-IP₆/PPF. The hXPR1-IP₆/PPF model is shown as a line drawing with no fill color, except for the TMH9a highlighted in red and blue for protomer A and B, respectively. (C) Enlarged view showing the gating residues in the structural superposition among two protomers in hXPR1-IP₆/WO₄, hXPR1-IP₆/PPF, and hXPR1-IP₆^A. (D) The structural superposition among the SPX domains in hXPR1-IP₆/WO₄ and hXPR1-IP₆/PPF, using the protomer B from both structures as the alignment references.



gating events (Fig. 5D), typified by brief openings and closures, further aligning with channel-like behavior. In contrast to the Pi influx mechanisms mediated by the SLC34 and SLC20 families of Na⁺-Pi cotransporters (23, 35), XPR1 demonstrated the capability to mediate both influx and efflux of Pi, responsive to the direction of membrane-potential gradients. However, the gating mechanism regulated by IPs/PP-IPs ensures that XPR1 remains closed when intracellular phosphate levels are low, thereby preventing phosphate loss. The conductance and regulatory mechanisms distinguish XPR1 as a dedicated phosphate exporting channel, functionally differentiating it from the other two subfamilies of Pi transporters.

The XPR1 channel's gating mechanism is intricately regulated by the structural dynamics of transmembrane helix 9a (TMH9a) along with two pivotal residues, W573 and E600, the latter playing a more crucial role in controlling Pi efflux. Furthermore, the formation of a narrow, negatively charged acidic zone by D398, D529, and D533 between the central site and the cytoplasmic entrance reinforces the regulation of Pi influx by XPR1. A more open conformation is observed in the presence of IP₆, which is consistent with increased Pi current

in electrophysiological assays after IP₆ treatment. After our work was submitted, Yan *et al.* reported a cryo-EM study including Pi-bound hXPR1 TMD structures in open and closed conformations, as well as a SPX-TMD structure in IP₆-bound, closed conformation. A three-substrate binding-sites model was proposed based on the Pi-bound, open conformation, with "Site 2" corresponding to the potential PPF binding site identified in our hXPR1-IP₆/PPF structure. The IP₆-bound SPX-TMD structure from Yan *et al.* aligns well with our hXPR1-IP₆/PPF structure in terms of overall architecture and interSPX site-only occupancy by IP₆, supporting our findings regarding the TMD-SPX site's preference for PP-IPs. The consistent findings across these studies—on open and closed conformations and the IP₆-binding mechanism—along with the biased IPs/PP-IPs binding site and intermediate conformations shown in our study, provide a comprehensive view of PP-IP-gated Pi efflux through the XPR1 channel.

Materials and methods

XPR1 protein expression and purification

The cDNA encoding human XPR1 (UniProt ID: Q9UBH6) was subcloned into a pcDNA3.4 vector, incorporating a Tobacco Etch Virus (TEV)

protease cleavage site, a FLAG-tag epitope, and an octahistidine (8× His) tag at the C terminus for facilitated purification and detection. Site-directed mutagenesis employing the Quikchange protocol was utilized to introduce specific mutations into the XPR1 sequence. Prior to their use in functional assays and structural elucidation, all the mutants and WT constructs were verified through Sanger sequencing to ensure sequence fidelity.

The construct was expressed in Expi293F cells (Thermo Fisher Scientific, A14527) cultured in a chemically defined Balanced CD 293 medium (CELL-WISE) at 37°C, supplied with 5% CO₂. The cells were transiently transfected with the expression plasmids using PEI MAX (Polysciences) at a density of about 2.2 × 10⁶ cells/ml. After 72 hours of culture, the transfected cells were harvested by centrifugation at 1500 × g for 10 min, and the resulting cell pellets were stored at -80°C until further use.

All protein purifications were performed at 4°C to ensure the stability and integrity of the proteins. The harvested cell pellets were initially lysed using a hypotonic lysis buffer (10 mM NaCl, 5 mM MgCl₂, 20 mM HEPES, pH 7.5, 0.5 mg/ml deoxyribonuclease I, 1 × protease inhibitor (MCE), 1 mg/ml iodoacetamide) with

a glass Dounce homogenizer. The lysate was then centrifuged at 45,000 × g for 25 min to collect the cell debris. Subsequent homogenization of the cell debris was done in a hypertonic buffer (1 M NaCl, 5 mM MgCl₂, 20 mM HEPES, pH 7.5, 0.5 mg/ml deoxyribonuclease I, 1× protease inhibitor) to further disrupt the cells, and the crude membrane fraction was isolated by centrifugation at 45,000 × g for 25 min. The membrane fraction was homogenized with a glass Douncer in a solubilization buffer (150 mM NaCl, 20 mM HEPES, pH 7.5, 1% (w/v) LMNG (Anatrace), 0.1% (w/v) cholestryl hemisuccinate (Anatrace), 10% (v/v) glycerol, 1× protease inhibitor), and solubilized for 2 hours at 4°C. The insolubles were removed by centrifugation (45,000 × g, 45 min). The supernatant was collected and subjected to affinity chromatography with anti-Flag resin (GeneScript), and the proteins of interest were eluted using elution buffer [150 mM NaCl, 20 mM HEPES, pH 7.5, 10% (v/v) Glycerol, 200 µg/ml 3 × flag peptide and 0.01% (w/v) glycol-diosgenin (GDN, Anatrace)]. Eluted proteins were further separated by SEC using Superose 6 Increase 10/300 GL column (Cytiva) in a mobile phase containing 150 mM NaCl, 20 mM HEPES, pH 7.5, and 0.01% (w/v) GDN. The fractions corresponding to the dimeric XPR1 proteins were pooled and concentrated to about 6.8 mg/ml for cryo-EM sample preparation.

With respect to the hXPR1 samples in the presence of IP₆ and PPF, 1 mM IP₆ (Sigma-Aldrich, P8810) and 10 mM PPF (Aladdin, P133387) were added after membrane homogenization. For the hXPR1-IP₆ sample, 1 mM IP₆ was added during purification. To prepare the hXPR1-IP₆/WO₄²⁻ sample, the hXPR1-IP₆ sample was further supplemented with 10 mM Na₂WO₄ (AR, 20042616) and incubated for 30 min before cryo-grids preparation. With regard to hXPR1-IP₇ sample, about 150 µM IP₇ was added during purification.

Electron microscopy sample preparation and data collection

Cryo-EM grids were prepared using Thermo Fisher Vitrobot Mark IV operated at 8°C with 100% humidity. hXPR1 with different additives and conditions were applied in 3-µl aliquot to glow-discharged holey carbon grids (Quantifoil R1.2/1.3, Au, 300 mesh). The sample was incubated with a grid for 10 s and blotted with filter paper (Waterman) for 1 s, then plunged into the liquid ethane and transferred with liquid nitrogen. Cryo-grids were subsequently checked using a 200-kV cryo-EM (FEI, Talos Arctica) to optimize protein concentration and particle quality.

High-resolution images were collected on a 300-kV cryo-EM (FEI, Titan Krios) equipped with a K3 Summit direct electron detector (Gatan), a Quantum energy filter (Gatan), and a Cs corrector (Thermo Fisher), operating in zero-energy

loss mode with a slit width of 15 eV. Movie stacks were automatically collected using EPU software at a magnification of 81,000 ×, corresponding to a physical pixel size of 1.1 Å, with a defocus range between -1.5 and -2.3 µm. The dose rate was set to approximately 16.26 electrons/Å² per second, and the total exposure time was 3.72 s, resulting in a total dose of 50 electrons/Å², fractionated into 32 frames.

Electron microscopy data processing

All cryo-EM data processing was conducted using RELION-3.1.1, RELION-4.0.1 and cryoSPARC-v4.0.1. Five datasets were collected, and the summary information is provided in table S1.

Motion correction was performed using MotionCorr2 with 12 × 10 patches, and CTF parameters were estimated using Gctf (36). Images with poor statistics were discarded. Particle picking was carried out using Gautomatch-v0.56 (<https://github.com/JackZhang-Lab/Gautmatch/>) or Topaz-v0.2.5 (37), and a subset of particles after 2D classification was utilized to generate initial references using the *Ab-Initio* Reconstruction module in cryoSPARC. For each full dataset, poor particles were excluded by two cycles of 2D classification at 4× binning. Subsequently, multi-rounds of Heterogeneous Refinement at 2× binning were conducted in cryoSPARC, and particles in the best class were re-extracted at a 1× binning pixel size. Bayesian polishing was performed in RELION-3.1.1 on the re-extracted particles. The polished particles were then subjected to cryoSPARC, followed by several rounds of Heterogeneous Refinement and Non-uniform Refinement to generate high-resolution maps. Local resolution estimation was performed using cryoSPARC's Local Resolution Estimation module, and all resolutions were estimated using the gold-standard Fourier shell correlation 0.143 criteria with high-resolution noise substitution.

For the datasets involving samples supplemented with IP₆ and PPF, particles were re-picked using a good reference, and particles with well-defined soluble domains were classified by seed-facilitated 3D classification. The re-picked and classified particles were then processed in cryoSPARC, undergoing several rounds of Heterogeneous Refinement. Particles lacking clearly resolved SPX domains were refined with C2 symmetry, accompanied by local CTF Refinement and Non-uniform Refinement, resulting in high-resolution maps. Particles with clearly defined SPX domains were processed in RELION, and re-picked particles based on the available SPX map. After several rounds of masked 3D classification, particles with clearly resolved defined SPX domains were further processed in cryoSPARC, undergoing Heterogeneous Refinement and Non-uniform Refinement in C2 symmetry to yield high-resolution maps showing density for XPR1 in full-length.

For datasets involving samples supplemented only with IP₆, polished particles were reclassified

with different K and T values by 3D Classification without alignment, resulting in three classes of particles with varied transmembrane domain conformations. These particles were then processed in cryoSPARC, with Non-uniform Refinement, resulting in three high-resolution maps with different transmembrane domain conformations.

For the datasets involving samples supplemented with IP₆ and WO₄²⁻, polished particles were classified by Heterogeneous Refinement using the three references from the IP₆-only dataset. After Non-uniform Refinement with clearly defined SPX domain particles, the final reconstruction yielded a 3.65 Å density map.

For the datasets involving samples supplemented with IP₇, polished particles were classified by 3D classification in RELION with alignment, followed by CTF Refinement and Non-uniform Refinement in C2 symmetry with clearly defined SPX domain particles, to yield 2.84-Å density maps showing density for XPR1 in full-length binding with 5-IP₇.

Model building and refinement

The model building for cryo-EM data of hXPR1 apo was performed with COOT (version 0.9.4.1) (38) using the AlphaFold predicted structure of hXPR1 as the starting model (<https://alphafold.ebi.ac.uk/entry/Q9UBH6>). The starting model was iteratively adjusted and refined with the Real-space refinement module in the Phenix package (version 1.20) (39) and Coot. For the model building for cryo-EM data of hXPR1 supplemented with IP₆, IP₆/PPF, IP₇, and IP₆/WO₄, the cryo-EM structure of hXPR1 apo served as the starting model. The small molecules, including IP₆, IP₇, PPF, and WO₄²⁻, were fit in the nonproteinous electron densities from their respective EM maps and refined using LigandFit and Real-space refinement modules in the Phenix package.

Electrophysiology assay

For the electrophysiological experiments, HEK293T cells were cultured in Dulbecco's modified Eagle's medium (DMEM) (Corning, USA) supplemented with 1% (w/v) penicillin/streptomycin (Gibco, USA), 1% (w/v) glutamate (Gibco), and 10% (v/v) fetal bovine serum (FBS) (PAN-Biotech GmbH, Germany) at 37°C in a humidified atmosphere containing 5% CO₂ and 95% air, following established protocols (40). WT human XPR1 and its mutants in the pcDNA3.4 vector were transfected into HEK293T cells together with PIRES2-EGFP using the lipid transfection reagent Lipo293TM (Beyotime). The transfected cells were allowed to culture for 24 hours before conducting the electrophysiological experiments.

All electrophysiological recordings were conducted at room temperature (23 ± 2°C) using an Axon 200B amplifier combined with a Digiatal1550 digitizer (Axon Instruments, USA) on HEK293T cells, as outlined in previous studies

(40). Patch-clamp experiments were performed on HEK293T cells displaying bright green fluorescence. Data acquisition and analysis were carried out using pCLAMP 10.7 software (Axon Instruments). For Pi currents, the bath solution contained 150 mM N-methyl-d-glucamine (NMDG), 100 mM H₃PO₄, 10 mM HEPES (pH 7.4), and the pipette solution contained 150 mM NMDG, 100 mM H₃PO₄, 10 mM HEPES, 10 mM EGTA. An additional 1 mM IP₆ was added to the pipette solution for experiments involving IP₆. The experimental setup utilized a step voltage protocol ranging from -180 mV to +100 mV with a +20-mV step for 1 to 3 min after achieving whole-cell configuration (34). Apparent affinity measurements for IP₆ and IP₇ in XPR1 were performed using inside-out macropatch recordings with Na⁺-free IPXs (free acid form) at concentrations ranging from 0.1 to 30 mM. Given that elevated intracellular Na⁺ levels significantly influence Pi permeability, we performed inside-out macropatch recordings to evaluate the anion selectivity of XPR1 using various Na⁺-free anion solutions, including NMDG-Cl⁻, NMDG-SO₄²⁻, and NMDG-NO₃⁻. Inhibitory effects of PPF (sodium phosphonoformate hexahydrate, Aladdin) were assessed using the same pipette and bath solutions.

The Goldman-Hodgkin-Katz (GHK) equation was employed to calculate membrane potential: $E_{rev}(Pi) = RT/F * \ln \frac{P_{Pi}[Pi]_i}{P_{Pi}[Pi]_o}$, $E_{rev}(Cl^-) = RT/F * \ln \frac{P_{Cl}[Cl]_i}{P_{Cl}[Cl]_o}$, $E_{rev}(NO_3^-) = RT/F * \ln \frac{P_{NO_3}[NO_3]_i}{P_{NO_3}[NO_3]_o}$, $E_{rev}(SO_4^{2-}) = RT/2F * \ln \frac{P_{SO_4}[SO_4]_i}{P_{SO_4}[SO_4]_o}$. Here, R denotes the gas constant (8.314 V·C·K⁻¹·mol⁻¹), T is the absolute temperature (set at 25°C for the experiments), and F represents the Faraday constant (9.648×10^4 C·mol⁻¹). We used the reversal potential values obtained from the Ramp protocol and input them into the GHK equation, with P (Pi) set to 1, to derive the relative ionic permeability values.

For single-channel recording, the data were acquired using an Axopatch 200B amplifier (Molecular Devices) in conjunction with a Digidata 1550B digitizer (Molecular Devices). Recording pipettes, fabricated from borosilicate glass (World Precision Instruments, Inc.) and fire-polished, exhibited resistances ranging from 8 to 12 megohms. Both the intracellular and extracellular solutions were composed of the same Pi solution. Prior to data acquisition, the amplifier was set to a holding potential of -80 mV. Single-channel recordings were performed using inside-out configurations, with signals sampled at 10 kHz, filtered at 2 kHz, and low-pass filtered at 300 Hz. Data analysis was conducted using Clampfit software (Molecular Devices).

Overexpression and purification of inositol hexakisphosphate kinase A (IP6KA) for chemoenzymatic synthesis of inositol pyrophosphates

The protocol was adopted from previously established protocols (27, 41). Briefly, a pET31

plasmid harboring the codon-optimized cDNA encoding *Entamoeba histolytica* IP6KA (UniProt ID: C4M387) was transformed into *Escherichia coli* BL21 (DE3) cells. Isopropyl β-D-1-thiogalactopyranoside (IPTG) was added to a final concentration of 0.1 mM when the cell density reached an OD₆₀₀ of approximately 0.6. The cell culture was then incubated at 16°C for 18 hours and harvested by centrifugation at 4000 g for 25 min.

The cell pellet was resuspended in a lysis buffer containing 150 mM NaCl, 20 mM HEPES (pH 7.4), 5 mM MgCl₂, 1 mM tris(2-carboxyethyl) phosphine (TCEP), and 50 mM imidazole. The cell suspension was supplemented with 0.5 mg/ml DNase I and a protease inhibitor mix (TargetMol), and lysed by sonication. The lysates were clarified by centrifugation at 45,000 g for 45 min at 4°C. The supernatants were filtered using a VWR® vacuum filter (PES, 0.45 μm) and loaded onto a Ni-SMART column (Smart-Lifesciences) equilibrated with the lysis buffer. The column was washed with the lysis buffer, and IP6KA was eluted with an elution buffer containing 150 mM NaCl, 20 mM HEPES (pH 7.4), 5 mM MgCl₂, 1 mM TCEP, and 300 mM imidazole. The eluents containing IP6KA were supplemented with 25% (v/v) glycerol and stored at -80°C.

Chemoenzymatic synthesis and purification of IP₇

The protocol was adopted from (27). Briefly, MilliQ water was prewarmed to 37°C by incubation in a water bath. A solution containing 3 mM IP₆, 20 mM MES (pH 6.4), 50 mM NaCl, 5 mM ATP (disodium salt), 10 mM creatine phosphate, 7 mM MgCl₂, and 1 mM DTT was prepared in 150 ml of prewarmed MilliQ water. This solution was incubated in a water bath at 37°C for 10 min. Subsequently, 14 mg of IP6KA and creatine kinase (1 U/ml) were added, and the conical flask was gently inverted several times to homogenize the solution. The reaction was left to proceed for 90 min without shaking.

Approximately 60 ml of wet Amberlite IRC-748 resin was sequentially washed with 1 liter of methanol and 1 liter of water, then stored at 4°C in a methanol:H₂O (1:4) mixture. Before use, the resin was washed with 1 liter of water, acidified with 500 ml of 1 M hydrochloric acid, and washed with water until the pH reached 6 to 7. The resin was then equilibrated with 500 ml of 1 M ammonium bicarbonate, washed with 1 liter of water, and air-dried for future use.

Fifteen grams of C₁₈ bonded silica gel (100-Å pore size, 30-μm particle size) was placed in a sintered glass funnel and covered with quartz sand. The silica gel was washed sequentially with 100 ml of acetonitrile and 100 ml of water. The reaction mixture (150 ml) was passed through the C₁₈ column, followed by washing the column with 200 ml of water. The eluate was collected, and 4.6 g (50 equivalents) of magnesium chloride hexahydrate was added. The pH was adjusted to 8.7 with 1 M NaOH,

and the mixture was allowed to precipitate at room temperature for 4 hours. After precipitation, the supernatant was removed by centrifugation at 3000 g for 2 min. The precipitate was washed thrice with 60 ml of 8 mM MgCl₂ solution at pH 9, then resuspended in 60 ml of 10 mM ammonium bicarbonate solution. Approximately 50 ml of pre-equilibrated Amberlite IRC-748 resin was added, and the mixture was vortexed until clear. The solution was passed through a 10-ml Amberlite IRC-748 cation exchange column equilibrated with NH₄⁺, and the column was washed with 40 ml of water. The eluate was collected and filtered through a 0.22 μm membrane, resulting in approximately 100 ml of clear solution, which was then lyophilized to obtain a white solid.

Electrophoresis analysis of inositol polyphosphates in chemoenzymatic synthesis

The protocol was adopted from (42, 43). Briefly, samples containing inositol polyphosphates were resolved using an 8.3 × 7.3 cm gel made with 33.3% polyacrylamide in TBE (Tris-Borate-EDTA) buffer. The gel preparation composition included 31.7 ml of 40% acrylamide/bisacrylamide (19:1), 3.8 ml of 10× TBE, 2.2 mL of H₂O, 270 μl of 10% ammonium persulfate (APS), and 30 μl of TEMED (N, N, N', N'-Tetramethylethylenediamine). Gels were pre-run at 300 V for 30 min. Samples were prepared by adding 5 to 10 μl of 6 × dye (10 mM Tris-HCl, pH 7.0; 1 mM EDTA; 30% glycerol; 0.1% Orange G) before loading onto the gels. Electrophoresis was performed at 300 V for 100 min. Gels were then gently agitated for 30 min at room temperature in a filtered staining solution containing 20% methanol, 2% glycerol, and 0.05% Toluidine Blue, followed by de-staining for 120 min with several changes of the same solution without dye.

REFERENCES AND NOTES

- M. W. Bowler, M. J. Cliff, J. P. Walther, G. M. Blackburn, Why did Nature select phosphate for its dominant roles in biology? *New J. Chem.* **34**, 784–794 (2010). doi: [10.1039/b9nj00718k](https://doi.org/10.1039/b9nj00718k)
- C. Azevedo, A. Sariardi, Eukaryotic Phosphate Homeostasis: The Inositol Pyrophosphate Perspective. *Trends Biochem. Sci.* **42**, 219–231 (2017). doi: [10.1016/j.tibs.2016.10.008](https://doi.org/10.1016/j.tibs.2016.10.008); pmid: [27876550](https://pubmed.ncbi.nlm.nih.gov/27876550/)
- G. R. Beck Jr., Inorganic phosphate as a signaling molecule in osteoblast differentiation. *J. Cell. Biochem.* **90**, 234–243 (2003). doi: [10.1002/jcb.10622](https://doi.org/10.1002/jcb.10622); pmid: [14505340](https://pubmed.ncbi.nlm.nih.gov/14505340/)
- M. J. Berridge, R. F. Irvine, Inositol phosphates and cell signalling. *Nature* **341**, 197–205 (1989). doi: [10.1038/341197a0](https://doi.org/10.1038/341197a0); pmid: [2550825](https://pubmed.ncbi.nlm.nih.gov/2550825/)
- S. Chande, C. Bergwitz, Role of phosphate sensing in bone and mineral metabolism. *Nat. Rev. Endocrinol.* **14**, 637–655 (2018). doi: [10.1038/s41574-018-0076-3](https://doi.org/10.1038/s41574-018-0076-3); pmid: [30218014](https://pubmed.ncbi.nlm.nih.gov/30218014/)
- A. Legati et al., Mutations in XPR1 cause primary familial brain calcification associated with altered phosphate export. *Nat. Genet.* **47**, 579–581 (2015). doi: [10.1038/ng.3289](https://doi.org/10.1038/ng.3289); pmid: [25938945](https://pubmed.ncbi.nlm.nih.gov/25938945/)
- C. M. Giachelli et al., Vascular calcification and inorganic phosphate. *Am. J. Kidney Dis.* **38**, S34–S37 (2001). doi: [10.1053/ajkd.2001.27394](https://doi.org/10.1053/ajkd.2001.27394); pmid: [11576919](https://pubmed.ncbi.nlm.nih.gov/11576919/)
- M. Levi et al., Mechanisms of phosphate transport. *Nat. Rev. Nephrol.* **15**, 482–500 (2019). doi: [10.1038/s41581-019-0159-y](https://doi.org/10.1038/s41581-019-0159-y); pmid: [31168066](https://pubmed.ncbi.nlm.nih.gov/31168066/)
- I. C. Forster, N. Hernando, J. Biber, H. Murer, Phosphate transporters of the SLC20 and SLC34 families. *Mol. Aspects*

- Med.* **34**, 386–395 (2013). doi: [10.1016/j.mam.2012.07.007](https://doi.org/10.1016/j.mam.2012.07.007); pmid: [23506879](https://pubmed.ncbi.nlm.nih.gov/23506879/)
10. L. V. Virkki, J. Biber, H. Murer, I. C. Forster, Phosphate transporters: A tale of two solute carrier families. *Am. J. Physiol. Renal Physiol.* **293**, F643–F654 (2007). doi: [10.1152/ajprenal.00228.2007](https://doi.org/10.1152/ajprenal.00228.2007); pmid: [17581921](https://pubmed.ncbi.nlm.nih.gov/17581921/)
 11. C. S. Tailor, A. Nouri, C. G. Lee, C. Kozak, D. Kabat, Cloning and characterization of a cell surface receptor for xenotropic and polytropic murine leukemia viruses. *Proc. Natl. Acad. Sci. U.S.A.* **96**, 927–932 (1999). doi: [10.1073/pnas.96.3.927](https://doi.org/10.1073/pnas.96.3.927); pmid: [9927670](https://pubmed.ncbi.nlm.nih.gov/9927670/)
 12. A. E. Vaughan, R. Mendoza, R. Aranda, J.-L. Battini, A. D. Miller, Xpr1 is an atypical G-protein-coupled receptor that mediates xenotropic and polytropic murine retrovirus neurotoxicity. *J. Virol.* **86**, 1661–1669 (2012). doi: [10.1128/JVI.06073.11](https://doi.org/10.1128/JVI.06073.11); pmid: [22090134](https://pubmed.ncbi.nlm.nih.gov/22090134/)
 13. D. Giovannini, J. Touhami, P. Charnet, M. Sitbon, J.-L. Battini, Inorganic phosphate export by the retrovirus receptor XPR1 in metazoans. *Cell Rep.* **3**, 1866–1873 (2013). doi: [10.1016/j.celrep.2013.05.035](https://doi.org/10.1016/j.celrep.2013.05.035); pmid: [23791524](https://pubmed.ncbi.nlm.nih.gov/23791524/)
 14. X. Li et al., Control of XPR1-dependent cellular phosphate efflux by InsP₈ is an exemplar for functionally-exclusive inositol pyrophosphate signaling. *Proc. Natl. Acad. Sci. U.S.A.* **117**, 3568–3574 (2020). doi: [10.1073/pnas.1908830117](https://doi.org/10.1073/pnas.1908830117); pmid: [32019887](https://pubmed.ncbi.nlm.nih.gov/32019887/)
 15. U. López-Sánchez et al., Characterization of XPR1/SLC53A1 variants located outside of the SPX domain in patients with primary familial brain calcification. *Sci. Rep.* **9**, 6776 (2019). doi: [10.1038/s41598-019-43255-x](https://doi.org/10.1038/s41598-019-43255-x); pmid: [31043717](https://pubmed.ncbi.nlm.nih.gov/31043717/)
 16. D. Secco et al., The emerging importance of the SPX domain-containing proteins in phosphate homeostasis. *New Phytol.* **193**, 842–851 (2012). doi: [10.1111/j.1469-8137.2011.04002.x](https://doi.org/10.1111/j.1469-8137.2011.04002.x); pmid: [22403821](https://pubmed.ncbi.nlm.nih.gov/22403821/)
 17. R. Wild et al., Control of eukaryotic phosphate homeostasis by inositol polyphosphate sensor domains. *Science* **352**, 986–990 (2016). doi: [10.1126/science.aad9858](https://doi.org/10.1126/science.aad9858); pmid: [27080106](https://pubmed.ncbi.nlm.nih.gov/27080106/)
 18. M. S. Wilson, T. M. Livermore, A. Saiardi, Inositol pyrophosphates: Between signalling and metabolism. *Biochem. J.* **452**, 369–379 (2013). doi: [10.1042/BJ20130118](https://doi.org/10.1042/BJ20130118); pmid: [23725456](https://pubmed.ncbi.nlm.nih.gov/23725456/)
 19. M. Bennett, S. M. Onnebo, C. Azevedo, A. Saiardi, Inositol pyrophosphates: Metabolism and signaling. *Cell. Mol. Life Sci.* **63**, 552–564 (2006). doi: [10.1007/s00018-005-5446-z](https://doi.org/10.1007/s00018-005-5446-z); pmid: [16429326](https://pubmed.ncbi.nlm.nih.gov/16429326/)
 20. M. S. Wilson, H. J. Jessen, A. Saiardi, The inositol hexakisphosphate kinases IP6K1 and -2 regulate human cellular phosphate homeostasis, including XPR1-mediated phosphate export. *J. Biol. Chem.* **294**, 11597–11608 (2019). doi: [10.1074/jbc.RA119.007848](https://doi.org/10.1074/jbc.RA119.007848); pmid: [31186349](https://pubmed.ncbi.nlm.nih.gov/31186349/)
 21. Y. Moritoh et al., The enzymatic activity of inositol hexakisphosphate kinase controls circulating phosphate in mammals. *Nat. Commun.* **12**, 4847 (2021). doi: [10.1038/s41467-021-24934-8](https://doi.org/10.1038/s41467-021-24934-8); pmid: [34381031](https://pubmed.ncbi.nlm.nih.gov/34381031/)
 22. R. Villa-Bellosta, V. Sorribas, Different effects of arsenate and phosphonoformate on P(i) transport adaptation in opossum kidney cells. *Am. J. Physiol. Cell Physiol.* **297**, C516–C525 (2009). doi: [10.1152/ajpcell.00186.2009](https://doi.org/10.1152/ajpcell.00186.2009); pmid: [19553564](https://pubmed.ncbi.nlm.nih.gov/19553564/)
 23. I. C. Forster, The molecular mechanism of SLC34 proteins: Insights from two decades of transport assays and structure-function studies. *Pflügers Arch.* **471**, 15–42 (2019). doi: [10.1007/s00424-018-2207-z](https://doi.org/10.1007/s00424-018-2207-z); pmid: [30244375](https://pubmed.ncbi.nlm.nih.gov/30244375/)
 24. A. Punjani, J. L. Rubinstein, D. J. Fleet, M. A. Brubaker, cryoSPARC: Algorithms for rapid unsupervised cryo-EM structure determination. *Nat. Methods* **14**, 290–296 (2017). doi: [10.1038/nmeth.4169](https://doi.org/10.1038/nmeth.4169); pmid: [28165473](https://pubmed.ncbi.nlm.nih.gov/28165473/)
 25. S. H. Scheres, RELION: Implementation of a Bayesian approach to cryo-EM structure determination. *J. Struct. Biol.* **180**, 519–530 (2012). doi: [10.1016/j.jsb.2012.09.006](https://doi.org/10.1016/j.jsb.2012.09.006); pmid: [23000701](https://pubmed.ncbi.nlm.nih.gov/23000701/)
 26. M. K. Ried et al., Inositol pyrophosphates promote the interaction of SPX domains with the coiled-coil motif of PHR transcription factors to regulate plant phosphate homeostasis. *Nat. Commun.* **12**, 384 (2021). doi: [10.1038/s41467-020-20681-4](https://doi.org/10.1038/s41467-020-20681-4); pmid: [33452263](https://pubmed.ncbi.nlm.nih.gov/33452263/)
 27. R. Puschmann, R. K. Harmel, D. Fiedler, Scalable Chemoenzymatic Synthesis of Inositol Pyrophosphates. *Biochemistry* **58**, 3927–3932 (2019). doi: [10.1021/acs.biochem.9b00587](https://doi.org/10.1021/acs.biochem.9b00587); pmid: [31461621](https://pubmed.ncbi.nlm.nih.gov/31461621/)
 28. B. P. Pedersen et al., Crystal structure of a eukaryotic phosphate transporter. *Nature* **496**, 533–536 (2013). doi: [10.1038/nature12042](https://doi.org/10.1038/nature12042); pmid: [23542591](https://pubmed.ncbi.nlm.nih.gov/23542591/)
 29. J. Y. Tsai et al., Structure of the sodium-dependent phosphate transporter reveals insights into human solute carrier SLC20. *Sci. Adv.* **6**, eabb4024 (2020). doi: [10.1126/sciadv.abb4024](https://doi.org/10.1126/sciadv.abb4024); pmid: [32821837](https://pubmed.ncbi.nlm.nih.gov/32821837/)
 30. K. E. Kishi et al., Structural basis for channel conduction in the pump-like channelrhodopsin ChRMine. *Cell* **185**, 672–689.e23 (2022). doi: [10.1016/j.cell.2022.01.007](https://doi.org/10.1016/j.cell.2022.01.007); pmid: [35141111](https://pubmed.ncbi.nlm.nih.gov/35141111/)
 31. K. Tucker, S. Sridharan, H. Adesnik, S. G. Brohawn, Cryo-EM structures of the channelrhodopsin ChRMine in lipid nanodiscs. *Nat. Commun.* **13**, 4842 (2022). doi: [10.1038/s41467-022-32441-7](https://doi.org/10.1038/s41467-022-32441-7); pmid: [35977941](https://pubmed.ncbi.nlm.nih.gov/35977941/)
 32. E. J. Levin et al., Structure and permeation mechanism of a mammalian urea transporter. *Proc. Natl. Acad. Sci. U.S.A.* **109**, 11194–11199 (2012). doi: [10.1073/pnas.1207362109](https://doi.org/10.1073/pnas.1207362109); pmid: [22733730](https://pubmed.ncbi.nlm.nih.gov/22733730/)
 33. G. Chi et al., Structural characterization of human urea transporters UT-A and UT-B and their inhibition. *Sci. Adv.* **9**, eadg8229 (2023). doi: [10.1126/sciadv.adg8229](https://doi.org/10.1126/sciadv.adg8229); pmid: [37774028](https://pubmed.ncbi.nlm.nih.gov/37774028/)
 34. B. Ma et al., A plasma membrane transporter coordinates phosphate reallocation and grain filling in cereals. *Nat. Genet.* **53**, 906–915 (2021). doi: [10.1038/s41588-021-00855-6](https://doi.org/10.1038/s41588-021-00855-6); pmid: [33927398](https://pubmed.ncbi.nlm.nih.gov/33927398/)
 35. L. V. Virkki, I. C. Forster, J. Biber, H. Murer, Substrate interactions in the human type IIa sodium-phosphate cotransporter (NaPi-IIa). *Am. J. Physiol. Renal Physiol.* **288**, F969–F981 (2005). doi: [10.1152/ajprenal.00293.2004](https://doi.org/10.1152/ajprenal.00293.2004); pmid: [1613617](https://pubmed.ncbi.nlm.nih.gov/1613617/)
 36. K. Zhang, Geff: Real-time CTF determination and correction. *J. Struct. Biol.* **193**, 1–12 (2016). doi: [10.1016/j.jsb.2015.11.003](https://doi.org/10.1016/j.jsb.2015.11.003); pmid: [26592709](https://pubmed.ncbi.nlm.nih.gov/26592709/)
 37. T. Bepler et al., Positive-unlabeled convolutional neural networks for particle picking in cryo-electron micrographs. *Nat. Methods* **16**, 1153–1160 (2019). doi: [10.1038/s41592-019-0575-8](https://doi.org/10.1038/s41592-019-0575-8); pmid: [31591578](https://pubmed.ncbi.nlm.nih.gov/31591578/)
 38. P. Emsley, K. Cowtan, Coot: Model-building tools for molecular graphics. *Acta Crystallogr. D Biol. Crystallogr.* **60**, 2126–2132 (2004). doi: [10.1107/S0907444909052925](https://doi.org/10.1107/S0907444909052925); pmid: [15572765](https://pubmed.ncbi.nlm.nih.gov/15572765/)
 39. P. D. Adams et al., PHENIX: A comprehensive Python-based system for macromolecular structure solution. *Acta Crystallogr. D Biol. Crystallogr.* **66**, 213–221 (2010). doi: [10.1107/S0907444909052925](https://doi.org/10.1107/S0907444909052925); pmid: [20124702](https://pubmed.ncbi.nlm.nih.gov/20124702/)
 40. M. Y. Sun et al., Vanilloid agonist-mediated activation of TRPV1 channels requires coordinated movement of the S1–S4 bundle rather than a quiescent state. *Sci. Bull.* **67**, 1062–1076 (2022). doi: [10.1016/j.scib.2022.02.016](https://doi.org/10.1016/j.scib.2022.02.016); pmid: [36546250](https://pubmed.ncbi.nlm.nih.gov/36546250/)
 41. H. Wang, E. F. DeRose, R. E. London, S. B. Shears, IP6K structure and the molecular determinants of catalytic specificity in an inositol phosphate kinase family. *Nat. Commun.* **5**, 4178 (2014). doi: [10.1038/ncomms5178](https://doi.org/10.1038/ncomms5178); pmid: [24956979](https://pubmed.ncbi.nlm.nih.gov/24956979/)
 42. O. Losito, Z. Szijgyarto, A. C. Resnick, A. Saiardi, Inositol pyrophosphates and their unique metabolic complexity: Analysis by gel electrophoresis. *PLOS ONE* **4**, e5580 (2009). doi: [10.1371/journal.pone.0005580](https://doi.org/10.1371/journal.pone.0005580); pmid: [19440344](https://pubmed.ncbi.nlm.nih.gov/19440344/)
 43. E. Riemer et al., ITPK1 is an InsP₆/ADP phosphotransferase that controls phosphate signaling in Arabidopsis. *Mol. Plant* **14**, 1864–1880 (2021). doi: [10.1016/j.molp.2021.07.011](https://doi.org/10.1016/j.molp.2021.07.011); pmid: [34274522](https://pubmed.ncbi.nlm.nih.gov/34274522/)
 44. B. K. Ho, F. Gruswitz, HOLLOW: Generating accurate representations of channel and interior surfaces in molecular structures. *BMC Struct. Biol.* **8**, 49 (2008). doi: [10.1186/1472-6807-8-49](https://doi.org/10.1186/1472-6807-8-49); pmid: [19014592](https://pubmed.ncbi.nlm.nih.gov/19014592/)

ACKNOWLEDGMENTS

We thank M. Lei, M. Zhou, and L. Wang (for scientific discussion).

Funding: This work was supported by the National Natural Science Foundation of China [82072468 and 82272519 (to Y.C.), 32371289 (to Y.Y.), 82130073 (to J.Z.), and 82372430 (to A.Q.)], the Shanghai Municipal Committee of Science and Technology [20SI1902000 to Y.C.], and the SHIPM-pi fund [JY201804 to Y.C. and J.Z.] from the Shanghai Institute of Precision Medicine, the Ninth People's Hospital, Shanghai Jiao Tong University School of Medicine, the Natural Science Foundation of Jiangsu Province [BK20202002 to Y.Y.], and the Innovation and Entrepreneurship Talent Program of Jiangsu Province (to Y.Y.). This work was also supported by the Class IV Peak Disciplines (Shanghai Institute of Precision Medicine), the Shanghai Frontiers Science Center of Degeneration and Regeneration, Skeletal Systems, and the Innovative Research Team of High-Level Local Universities (SHSMU-ZLX2021700) from the Shanghai Municipal Education Commission. We thank the staff members of the Electron Microimaging Center, Bioimaging Facility, and Proteomics Platform at the Shanghai Institute of Precision Medicine for providing technical support and assistance in data collection. **Author contributions:** Y.C. and Y.Y. conceived the study. Y.C., Y.Y., Y.L., L.Z., C.-X.Y., Q.Z., Y.X., D.Y., and C.-R.G. designed the experiments. Y.Y., C.-X.Y., and C.-R.G. performed the electrophysiological assay. Y.L., L.Z., Q.Z., X.Y., S.L., M.C., and Y.C. performed structural biology experiments. Y.C., Y.L., and D.Y. built and refined the structural models. Y.L., X.Z., Y.C., and L.Z. performed chemoenzymatic synthesis. Y.C., Y.L., L.Z., Y.Y., C.-X.Y., J.Z., and A.Q. wrote the manuscript. **Competing interests:** The authors declare that they have no competing interests. **Data and materials availability:** The coordinates and the cryo-EM maps in this manuscript are deposited at the Protein Data Bank (PDB) and the Electron Microscopy Data Bank (EMDB) with accession codes: 8YEX and EMD-3920 for hXPR1 apo, 8YET and EMD-39203 for XPR1-IP_e/PPF, 8YFW and EMD-3923 for XPR1-IP_e/WO₄, 8YFU and EMD-39230 for XPR1-IP_e/WO₄ local refinement, 8YFD and EMD-39220 for dimeric XPR1^{II}, 8YF4 and EMD-3922 for asymmetric XPR1^{open/II}, and 9IWS and EMD-60962 for XPR1-IP_e. All other data are presented in the main text or supplementary materials. **License information:** Copyright © 2024 the authors, some rights reserved; exclusive licensee American Association for the Advancement of Science. No claim to original US government works. <https://www.science.org/about/science-licenses-journal-article-reuse>

SUPPLEMENTARY MATERIALS

science.org/doi/10.1126/science.adp3252

Figs. S1 to S17

Tables S1 to S3

Movie S1

MDAR Reproducibility Checklist

Submitted 20 March 2024; resubmitted 12 August 2024

Accepted 16 September 2024

Published online 26 September 2024